This manuscript is a non-peer-reviewed preprint submitted to EarthArXiv.

It has been submitted to Geochemical Perspectives Letters for peer review.

Classifying rock dissolution patterns using reaction persistence length and front velocity

Atefeh Vafaie[1*], Samuel Krevor[2]

[1]Global Change Research Group (GCRG), Mediterranean Institute for Advanced Studies (IMEDEA-CSIC-UIB), Esporles, Spain

[2]Department of Earth Science and Engineering, Imperial College London, London SW7 2AZ, United Kingdom

Corresponding author's email: atefeh.vafaie@csic.es

Abstract

Acid–rock dissolution in carbonates underpins many natural and engineered subsurface processes. Péclet–Damköhler (*Pe–Da*) scaling is traditionally used to relate dissolution patterns to reaction kinetics, advection, and diffusion, but it fails to explain contrasting patterns in fluid–rock systems with similar pH. This is because *Da* does not capture reaction-rate changes along the flow path, and the framework omits reaction capacity, which varies widely among fluid–mineral systems. Here we revisit this problem by retaining *Pe* to describe the advection–diffusion balance, replacing *Da* with a reactive persistence length (L_E) representing the spatial extent of sustained reactivity, and introducing a reaction-front velocity (V_f) incorporating reaction capacity to describe front advance. Applying this framework to published experiments involving CO_2-rich water, HCl, and EDTA injection into limestone and undersaturated brine injection into salt reveals a common progression of dissolution patterns in three-dimensional Pe–L_E–V_f space despite chemical and mineralogical differences. These complementary physical measures capture both reactive-front advance and the spatial persistence of reactivity.

This manuscript is a non-peer-reviewed preprint submitted to EarthArXiv.

It has been submitted to Geochemical Perspectives Letters for peer review.

Keywords: Geological CO_2 storage; Reactivity persistence scale; Reaction front velocity; Dissolution regime

Introduction

Acid-rock interactions leading to matrix dissolution in carbonate rocks are important in natural and engineering subsurface processes, including but not limited to karstification (Frisia and Borsato, 2010), rock diagenesis (Machel, 1999), dolomitisation (Machel, 2004), carbonate acidising (Fredd and Fogler, 1998b), and acid mine drainage (Dold, 2017). These interactions also matter in geological CO_2 storage (Bachu, 2003), where dissolved CO_2 produces carbonic acid that reacts with carbonate minerals, potentially altering pore structure and flow properties (Gaus, 2010; Vialle et al., 2014; Vafaie et al., 2023a). These reactions generate distinct patterns: uniform matrix dissolution, ramified porosity fingers or wormholes, and a spatially broad porosity wave progressing through the rock, known as compact dissolution. These patterns can govern the evolution of flow pathways, permeability, and reactive surface area. Forecasting dissolution regimes requires a quantitative understanding of how fluid reactivity evolves during transport through heterogeneous rock pore structures (Phillips et al., 2020; Vafaie et al., 2025).

Dissolution patterns are conventionally classified in a dimensionless parameter space defined by the Péclet (*Pe*) and Damköhler (*Da*) numbers, which describe the relative importance of advection, diffusion, and reaction rates (Golfier et al., 2002; Fredd and Fogler, 1998b). A leading practical approach used in industry known as the global wormholing model is focused on empirical correlations between interstitial fluid velocity and the pore volumes required for wormhole breakthrough in a specific rock–fluid system (Buijse and Glasbergen, 2005; Talbot and Gdanski,

2008; Snippe et al., 2017; Snippe et al., 2020). Identifying fluid velocity as a key control on wormhole formation has been of value to these applications because injection rates are controlled by project operators.

However, reliance on the empirical global wormholing model reflects the limited applicability of *Pe–Da* scaling across chemically distinct fluid–rock systems. Reaction rates change as fluid progresses through a domain, while systems differ substantially in their total reaction capacity before equilibrium is reached (Fredd and Fogler, 1998a,b; Vafaie et al., 2023b; Golfier et al., 2002). Conventionally, a single Damköhler number calculated from inlet chemistry and initial reaction properties characterises the entire rock domain (Noiriel et al., 2009; Vialle et al., 2014). Yet fluid progressively approaches equilibrium with the dissolving mineral, and changes in fluid composition and pore structure produce spatially varying dissolution rates (Kurganskaya and Luttge, 2021; Hale et al., 2022; Noiriel et al., 2009; Vafaie et al., 2023b). The finite penetration lengths of porosity fingers and compact dissolution fronts reflect this progressive loss of reactivity along the flow path. Thus, an inlet- or upstream-defined *Da* captures the initial transport-reaction balance but neither downstream reactivity evolution nor reaction capacity. Consistent with this limitation, CO_2-rich water and HCl injection into carbonates (Vafaie et al., 2023b), EDTA injection into limestone (Fredd and Fogler, 1998b), and NaCl undersaturation experiments in salt packs (Golfier et al., 2002) produce similar dissolution patterns in different regions of conventional *Pe–Da* space (Fig. 1).

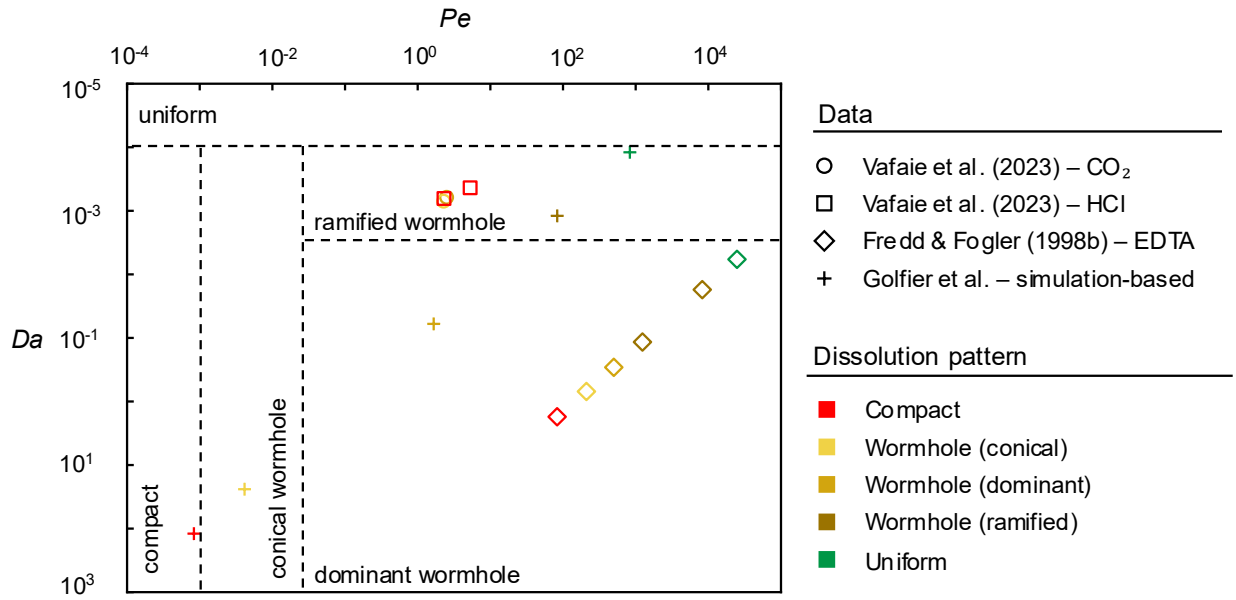


Figure 1. Dissolution patterns from literature data plotted on the *Pe-Da* regime diagram of Golfier et al. (2002). Colours indicate the observed dissolution patterns in the experiments, including compact, conical (C), dominant (D), and ramified (R) wormholing, as well as uniform dissolution. The regime boundaries originate from a Darcy-scale numerical model based on mass-transfer-limited dissolution. Salt-pack experiments reported by Golfier et al. (2002) fall within these fields, reflecting the consistency between the model assumptions and the NaCl dissolution system. In contrast, carbonate rock-acid systems involving CO_2-rich water, HCl, and EDTA yield markedly different dissolution morphologies.

In this study, we extend the current dissolution regime framework to incorporate reaction capacity alongside reaction kinetics and advective and diffusive transport behaviours, using physically based quantities that naturally emerge from the fluid dynamics involved in geological reactive transport. This involves replacing the Damköhler number with two complementary

quantities, known as the equilibration or reaction length and the reaction front velocity, and most commonly used in the field of geological fluid dynamics, that reflect the balance of reaction capacity and reaction kinetics against advective transport. These quantities are defined formally below. We use this framework to reanalyse literature data spanning a range of fluid-rock systems, including CO_2-rich water, HCl, and EDTA solutions interacting with limestones, as well as NaCl undersaturation experiments on salt packs (Fredd and Fogler, 1998; Golfier et al., 2002; Snippe et al., 2020; Vafaie et al., 2023b). We show that the framework resolves current discrepancies in mapping dissolution regimes onto observed reaction patterns across a wide range of experimental fluid and mineral environments.

Theory and Conceptual Framework

Here, we revisit the framework for forecasting dissolution regimes by retaining the Péclet number as a descriptor of advective–diffusive transport and replacing the Damköhler number with two complementary quantities: the equilibration length or reaction length, L_E, and the reaction-front velocity, V_f, both commonly used in the field of geological fluid dynamics (Phillips, 2009). These quantities separate the effects of reaction kinetics and fluid reaction capacity, which are combined within the conventional Damköhler number.

The Péclet number describes the relative importance of advective and diffusive transport (Oelkers, 1996),

$$Pe = qL/\varphi \cdot D, \quad (1)$$

where q is the Darcy flux (m s^{-1}), L is the characteristic flow length (m), φ is the rock porosity (-), and D is the effective diffusion coefficient (m^2 s^{-1}).

In Phillips' (2009) formulation, the reaction source is parameterised using a bulk rate coefficient, γ, with units of inverse time (s^{-1}). The corresponding reaction timescale is γ^{-1}. A fluid element moving at the mean interstitial velocity, u (m s^{-1}) travels the characteristic distance,

$$L_E = v/\gamma, \tag{2}$$

during this time. Therefore L_E (m), known as the reaction front width, is the distance over which the fluid approaches equilibrium with the solid. We will also refer to this as the reaction persistence length to better reflect the focus of its use in this analysis.

Equivalent bulk rate coefficients γ are not conventionally reported for fluid-mineral systems included in the present dataset. Calculating them would also require estimates of the accessible reactive surface area, which are uncertain and not reported consistently among the experiments (Noiriel et al., 2009). We therefore use a proxy of the reaction persistence length scale calculated as,

$$L_E = v/k_r, \tag{3}$$

where k_r is the more conventionally used reaction rate constant adopted for the relevant fluid-mineral system at the experimental temperature and fluid composition.

For proton-promoted carbonate dissolution, the reaction-rate constant is written as,

$$k_\mathrm{r} = k(T) \cdot 10^{-pH}, \tag{4}$$

where $k(T)$ is the temperature-dependent coefficient for the proton-promoted reaction mechanism (s^{-1}). The kinetic parameters used to evaluate $k(T)$ are taken from Palandri and Kharaka (2004) and 10^{-pH} represents the hydrogen-ion activity of the inlet fluid. For the EDTA–calcite system, the surface kinetic parameter is calculated from the values reported by Fredd and Fogler (1998c), for the protonated EDTA species dominant at pH 4. For the undersaturated NaCl system, the halite kinetic parameters are taken from Palandri and Kharaka (2004) and corrected to the experimental temperature using the Arrhenius equation.

Because k_{r} is not necessarily equivalent to the bulk equilibration coefficient γ used by Phillips (2009), we use L_E as a comparative measure of the reactivity persistence rather than the thickness of the reaction zone, although these properties should be proportional to each other. Low L_E values indicate that the reaction is rapid relative to advection, causing fluid reactivity to be consumed close to the inlet. High $L_E$values indicate that advection is rapid relative to reaction kinetics, allowing the fluid to remain reactive farther along the flow path.

Adopting the concept of reaction-front propagation driven by fluid supply and stoichiometric consumption (Phillips, 2009), the propagation of the reactive zone is captured by the reaction-front velocity,

$$V_f = q \cdot C_{max}/m.n, \tag{5}$$

where C_{max} is the maximum fluid reaction capacity under the given chemical conditions (mol m^{-3}), m is the stoichiometric coefficient representing the number of moles of reactant consumed per

mole of mineral dissolved, and n is the solid molar density (mol m^{-3}), which specifies the amount of dissolvable solid per unit bulk volume as,

$$n = \rho_s(1-\varphi)/M_s \quad (6)$$

where M_s is the molar mass (kg mol^{-1}) and ρ_s the density (kg m^{-3}).

We demonstrate this predictive framework against experimental data from the literature. A key parameter in this evaluation is $C_{\max}$, which depends on the fluid–rock system and is defined consistently:

- for strong-acid systems (HCl), as the inlet proton concentration, assuming complete consumption of acidity according to reaction stoichiometry,
- for CO_2-rich systems, C_{max} is defined as the equilibrium calcite dissolution capacity of the injected fluid at the imposed temperature and CO_2 pressure. This value is calculated from the increase in dissolved calcium between the CO_2-equilibrated inlet solution and the solution after equilibrium with calcite. PHREEQC calculations give C_{max} = 24.8 (mol m^{-3}) for the conditions of Vafaie et al. (2023b) and 23.92 (mol/m^3) for the single-phase experiments of Snippe et al. (2020).
- for EDTA systems, as the inlet chelating agent concentration, assuming a 1:1 stoichiometric complexation with calcium, and
- for NaCl undersaturation experiments, as the saturation deficit, i.e., the difference between the equilibrium solubility and the inlet concentration.

As such, $C_{\max}$ provides a consistent measure of the fluid's capacity to dissolve minerals across different chemistries.

Data and Analysis Approach

We integrate published dissolution experiments spanning a range of fluid-rock systems to assess how reactive length scale and reaction-front velocity describe the evolution of dissolution patterns. The dataset includes (i) CO_2-rich water and HCl interactions with Pont du Gard limestone (Vafaie et al., 2023b), (ii) single-phase CO_2-rich water injection into Estaillades limestone (Snippe et al., 2020), (iii) NaCl undersaturation experiments in Hele-Shaw salt packs (Golfier et al., 2002), and (iv) EDTA injection into Indiana limestone (Fredd and Fogler, 1998). For the Snippe et al. (2020) dataset, we include only the three single-phase experiments that reached wormhole breakthrough. We exclude the experiment without observed breakthrough and all multiphase experiments.

For each experiment, the Péclet number, Pe, is calculated from the measured flow rate, characteristic flow length, porosity, and effective diffusion coefficient. The reaction-rate constant, k_{r}, and maximum fluid reaction capacity, C_{max}, are determined using the system-specific definitions described above. The reactivity persistence scale, L_E, is then calculated from the measured flow rate, porosity, and reaction-rate constant, while the reaction-front velocity, V_f, is calculated from the measured flow rate, C_{max}, the solid molar density of the dissolving mineral, n, and the appropriate stoichiometric coefficient, m. Dissolution patterns reported in the original studies (compact, wormholing, dominant, ramified, or uniform) are retained without reinterpretation. A summary of the calculations is provided in Table 1.

172 **Table 1.** Summary of literature experiments reanalysed in this study. Parameters include rock
173 type, injected solution, pH, initial porosity (φ), Darcy flux (q), Péclet number (Pe) reaction rate
174 constant (k_r), maximum fluid reaction capacity (C_{max}), reactivity persistence scale (L_E), reaction-
175 front velocity (V_f), and dissolution pattern (DP). Dissolution patterns include compact (C), conical
176 wormholes (CW), dominant wormholes (DW), ramified wormholes (RW), and uniform dissolution
177 (U), as reported in the original studies.

Study	Rock	Solution	pH	φ (-)	q (m s^{-1})	Pe	C_{max} (mol m^{-3})	k_r (1 s^{-1})	L_E (m)	V_f (m s^{-1})	DP
Vafaie et al. (2023b)											
	L	CO_2	3.1	0.29	$5.1 \cdot 10^{-6}$	255	24.8	$6.8 \cdot 10^{-6}$	$2.6 \cdot 10^{-2}$	$6.7 \cdot 10^{-9}$	DW
	L	CO_2	3.1	0.24	$5.1 \cdot 10^{-6}$	224	24.8	$6.8 \cdot 10^{-6}$	$3.1 \cdot 10^{-2}$	$6.3 \cdot 10^{-9}$	CW
	L	HCl	3.1	0.26	$5.1 \cdot 10^{-6}$	381	7	$6.8 \cdot 10^{-6}$	$2.9 \cdot 10^{-2}$	$9.1 \cdot 10^{-10}$	C
	L	HCl	3.1	0.29	$5.1 \cdot 10^{-6}$	397	7	$6.8 \cdot 10^{-6}$	$2.6 \cdot 10^{-2}$	$9.4 \cdot 10^{-10}$	C
Snippe et al.(2020)											
	L	CO_2	3.2	0.28	$1.8 \cdot 10^{-6}$	135	23.92	$5.2 \cdot 10^{-4}$	$1.2 \cdot 10^{-2}$	$2.2 \cdot 10^{-9}$	DW
	L	CO_2	3.2	0.26	$4.0 \cdot 10^{-6}$	303	23.92	$5.2 \cdot 10^{-4}$	$3.0 \cdot 10^{-2}$	$4.8 \cdot 10^{-9}$	RW
	L	CO_2	3.2	0.27	$2.0 \cdot 10^{-5}$	$1.5 \cdot 10^{3}$	23.92	$5.2 \cdot 10^{-4}$	$1.4 \cdot 10^{-1}$	$2.4 \cdot 10^{-8}$	RW
Golfier et al. (2002)											
	S	NaCl	-	0.36	$2.8 \cdot 10^{-5}$	$6.9 \cdot 10^{3}$	5.3	0.598	$1.3 \cdot 10^{-4}$	$6.2 \cdot 10^{-9}$	C
	S	NaCl	-	0.36	$2.8 \cdot 10^{-4}$	$6.9 \cdot 10^{4}$	5.3	0.598	$1.3 \cdot 10^{-3}$	$6.2 \cdot 10^{-8}$	CW
50 g/l	S	NaCl	-	0.36	$4.4 \cdot 10^{-4}$	$1.1 \cdot 10^{5}$	5.3	0.598	$2.1 \cdot 10^{-3}$	$9.9 \cdot 10^{-8}$	CW
	S	NaCl	-	0.36	$5.5 \cdot 10^{-4}$	$1.3 \cdot 10^{5}$	5.3	0.598	$2.6 \cdot 10^{-3}$	$1.2 \cdot 10^{-7}$	DW
	S	NaCl	-	0.36	$1.1 \cdot 10^{-3}$	$2.7 \cdot 10^{5}$	5.3	0.598	$5.2 \cdot 10^{-3}$	$2.5 \cdot 10^{-7}$	RW
	S	NaCl	-	0.36	$1.4 \cdot 10^{-3}$	$3.5 \cdot 10^{5}$	5.3	0.598	$6.4 \cdot 10^{-3}$	$3.1 \cdot 10^{-7}$	RW
	S	NaCl	-	0.36	$2.8 \cdot 10^{-5}$	$6.9 \cdot 10^{3}$	3.59	0.598	$1.3 \cdot 10^{-4}$	$4.2 \cdot 10^{-9}$	C
	S	NaCl	-	0.36	$2.8 \cdot 10^{-4}$	$6.9 \cdot 10^{4}$	3.59	0.598	$1.3 \cdot 10^{-3}$	$4.2 \cdot 10^{-8}$	CW
150 g/l	S	NaCl	-	0.36	$4.4 \cdot 10^{-4}$	$1.1 \cdot 10^{5}$	3.59	0.598	$2.1 \cdot 10^{-3}$	$6.8 \cdot 10^{-8}$	DW
	S	NaCl	-	0.36	$5.5 \cdot 10^{-4}$	$1.3 \cdot 10^{5}$	3.59	0.598	$2.6 \cdot 10^{-3}$	$8.5 \cdot 10^{-8}$	DW
	S	NaCl	-	0.36	$1.1 \cdot 10^{-3}$	$2.7 \cdot 10^{5}$	3.59	0.598	$5.2 \cdot 10^{-3}$	$1.7 \cdot 10^{-7}$	RW
	S	NaCl	-	0.36	$1.4 \cdot 10^{-3}$	$3.4 \cdot 10^{5}$	3.59	0.598	$6.4 \cdot 10^{-3}$	$2.1 \cdot 10^{-7}$	RW
	S	NaCl	-	0.36	$8.3 \cdot 10^{-5}$	$2.1 \cdot 10^{4}$	2.22	0.598	$3.9 \cdot 10^{-4}$	$7.8 \cdot 10^{-9}$	C/CW
	S	NaCl	-	0.36	$1.6 \cdot 10^{-4}$	$4.1 \cdot 10^{4}$	2.22	0.598	$7.7 \cdot 10^{-4}$	$1.6 \cdot 10^{-8}$	C/CW
230 g/l	S	NaCl	-	0.36	$2.8 \cdot 10^{-4}$	$6.9 \cdot 10^{4}$	2.22	0.598	$1.3 \cdot 10^{-3}$	$2.6 \cdot 10^{-8}$	DW
	S	NaCl	-	0.36	$5.5 \cdot 10^{-4}$	$1.3 \cdot 10^{5}$	2.22	0.598	$2.6 \cdot 10^{-3}$	$5.2 \cdot 10^{-8}$	RW
	S	NaCl	-	0.36	$1.4 \cdot 10^{-3}$	$3.4 \cdot 10^{5}$	2.22	0.598	$6.4 \cdot 10^{-3}$	$1.3 \cdot 10^{-7}$	RW
	S	NaCl	-	0.36	$1.7 \cdot 10^{-3}$	$4.1 \cdot 10^{5}$	2.22	0.598	$7.7 \cdot 10^{-3}$	$1.6 \cdot 10^{-7}$	RW
Fredd and Fogler (1998b)											
	L	EDTA	4	0.18	$1.5 \cdot 10^{-7}$	15	250	$6.7 \cdot 10^{-4}$	$1.22 \cdot 10^{-3}$	$1.7 \cdot 10^{-9}$	C
	L	EDTA	4	0.18	$3.7 \cdot 10^{-7}$	37	250	$6.7 \cdot 10^{-4}$	$3.0 \cdot 10^{-3}$	$4.1 \cdot 10^{-9}$	CW
	L	EDTA	4	0.18	$8.8 \cdot 10^{-7}$	88	250	$6.7 \cdot 10^{-4}$	$7.3 \cdot 10^{-3}$	$9.9 \cdot 10^{-9}$	DW
	L	EDTA	4	0.18	$2.2 \cdot 10^{-6}$	220	250	$6.7 \cdot 10^{-4}$	$1.8 \cdot 10^{-2}$	$2.5 \cdot 10^{-8}$	RW
	L	EDTA	4	0.18	$1.5 \cdot 10^{-5}$	$1.4 \cdot 10^{3}$	250	$6.7 \cdot 10^{-4}$	$1.2 \cdot 10^{-1}$	$1.7 \cdot 10^{-7}$	RW
	L	EDTA	4	0.18	$4.4 \cdot 10^{-5}$	$4.4 \cdot 10^{3}$	250	$6.7 \cdot 10^{-4}$	$3.6 \cdot 10^{-1}$	$5.0 \cdot 10^{-7}$	U

178

Results and Discussion

When dissolution behaviour from all analysed studies is expressed in terms of reaction-front velocity (V_f), reactivity persistence scale (L_E), and Péclet number (Pe), the data form a coherent pattern across different fluid-rock systems (Fig. 2). This organisation is consistent across the diversity of chemistries considered and despite the wide range of dissolution morphologies originally reported. Dissolution regimes occupy distinct regions within the $L_E - V_f - \mathrm{P_e}$ space.

The correlation is the most sensitive to variation in $L_E - V_f$, forming a diagonal sequence from compact to wormholing and ultimately to uniform dissolution with increasing L_E and V_f. Compact dissolution is confined to low reactivity persistence scales and front velocities, where fluid reactivity is consumed near the inlet and the reactive front advances slowly. As L_E and V_f increase, the fluid remains reactive over a greater distance and supplies sufficient reaction capacity for localised dissolution pathways to develop. Within this intermediate region, the wormhole morphologies show a general progression from conical to dominant and then ramified structures. At the highest L_E and V_f , reactivity persists over a longer distance in the porous medium, and the reaction front advances more rapidly, favouring distributed and ultimately uniform dissolution.

The impact of the Péclet number is less strong across the parameter space. Figure 2 shows that although Pe provides insight into the balance between advective and diffusive transport, it does not clearly distinguish dissolution regimes. Similar dissolution patterns occur over broad and partly overlapping ranges of Pe. Within individual experimental datasets, increasing flow rate generally increases Pe, L_E, and V_f, promoting a progression towards more spatially distributed dissolution. However, this does not imply that Pe has a negligible influence. Extending the Pe

range within individual fluid–rock systems would help determine how stronger diffusive redistribution at lower Pe and stronger advective transport at higher Pe modify the regime organisation.

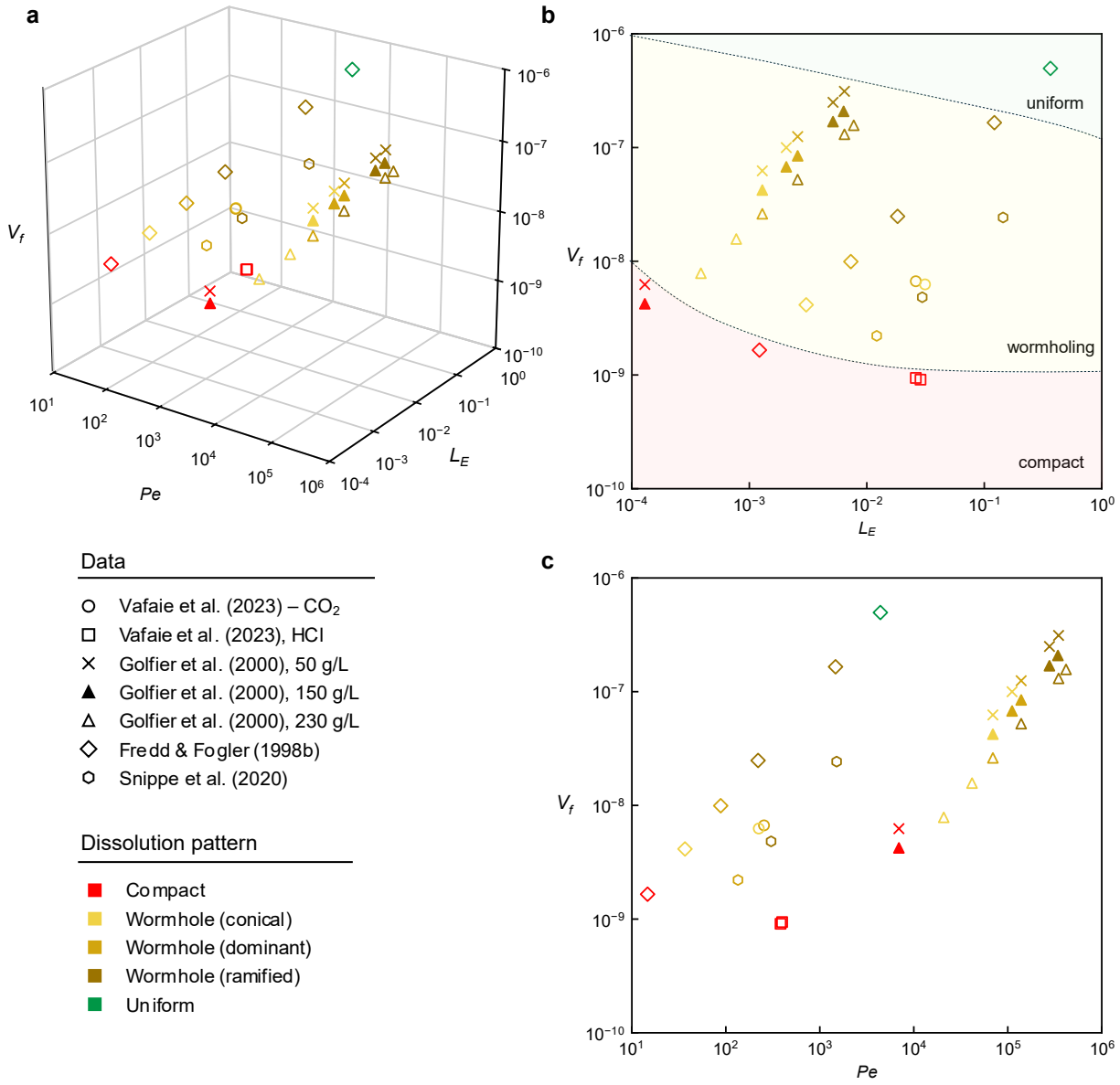


Figure 2. Distribution of dissolution patterns in terms of the Péclet number (*Pe*), reactivity persistence scale (L_E) , and reaction-front velocity (V_f) for carbonate and salt dissolution experiments. The dataset includes aqueous solutions with dissolved CO_2, HCl, and EDTA injected into limestone samples, as well as undersaturated aqueous NaCl solutions injected into salt packs. (a) Three-dimensional representation of the experimental data in Pe–L_E–V_f space. (b) Projection onto the L_E–V_f plane. (c) Projection onto the Pe–V_f plane. Marker shapes identify the experimental datasets, while marker colours represent the reported dissolution patterns. The shaded background regions indicate the broad progression from compact dissolution through wormholing to uniform dissolution. The boundaries between these regions illustrate the organisation of the experimental data and the inference of general regime boundaries.

The consistent spatial organisation of the data indicates a common physical control arising from combined effects of reaction kinetics, fluid reaction capacity, and advective transport, directly linking to the dissolution morphology. Figure 3 illustrates the mechanistic interpretation of this framework. At low L_E and V_f, reaction rapidly consumes the available fluid reactivity near the inlet, while the limited supply of reaction capacity results in slow propagation of the reactive zone. These conditions produce compact dissolution (Fig. 3b). At intermediate L_E and V_f fluid reactivity persists farther into the porous medium and the reactive zone advances more rapidly. Under these conditions, small variations in pore structure and permeability can direct the reactive flow into preferential pathways, promoting wormhole formation (Fig. 3c). At high L_E and V_f values, reactive fluid is transported over larger distances, and sufficient reaction capacity is supplied to

advance the front across a broader area. Consequently, dissolution becomes less localised and approaches a uniform regime (Fig. 3d).

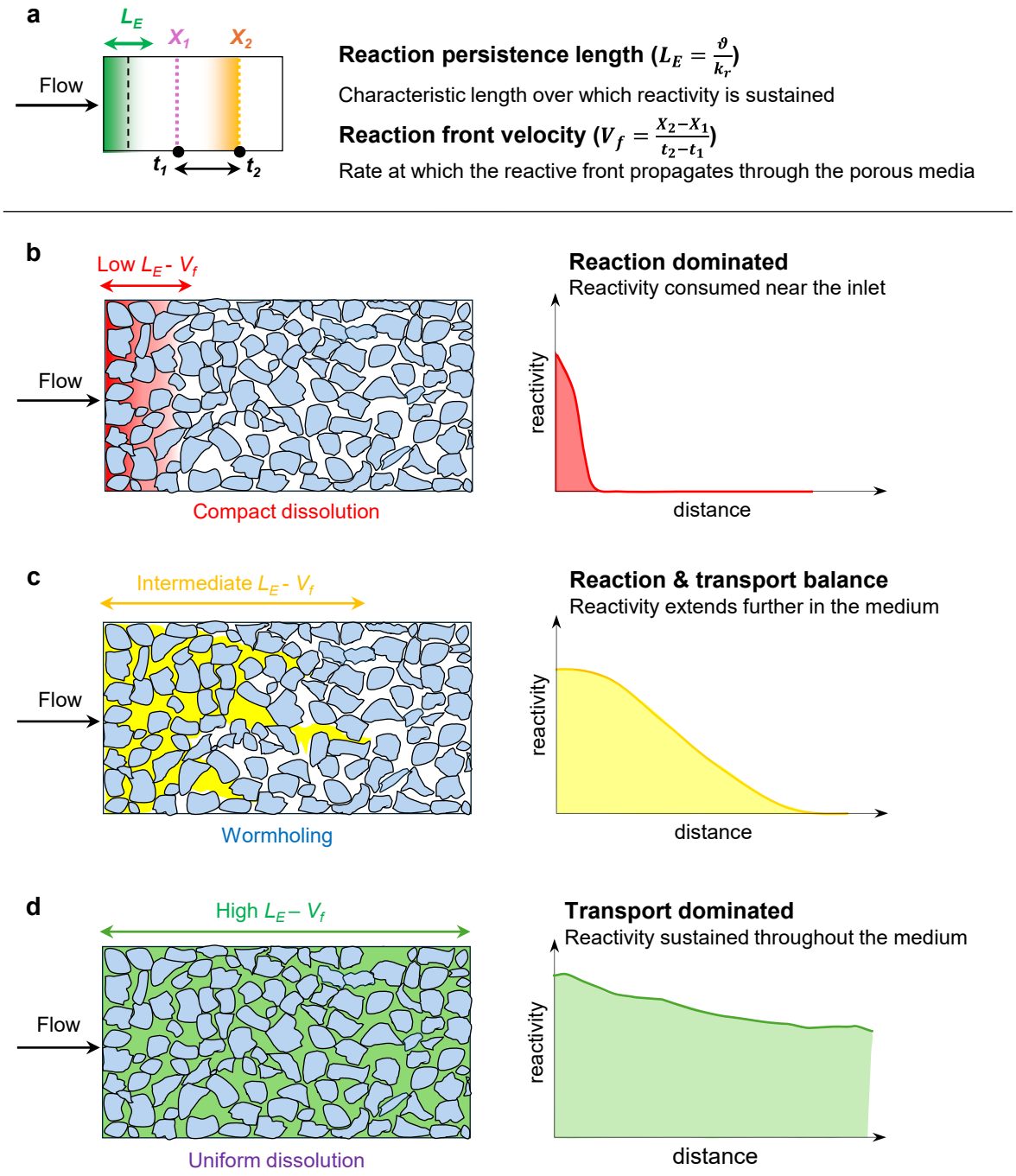


Figure 3. Conceptual illustration of transport–reaction coupling in porous media. (a) Reactivity persistence scale (L_E) and reaction-front velocity (V_f) defenition, where L_E represents the spatial extent over which reactivity is sustained, and V_f quantifies front propagation rate between two front positions (x_1 and x_2). (b) Low $L_E - V_f$: reaction dominates over transport, leading to compact dissolution. (c) Intermediate $L_E - V_f$: transport and reaction are balanced, promoting localised flow and wormhole formation. (d) High $L_E - V_f$: transport sustains reactivity over longer distances, resulting in more distributed and uniform dissolution.

Additional experiments would allow the framework to be tested for wider range of conditions, particularly for carbonate systems interacting with CO_2-rich fluids, for which the available data remain relatively limited (Vialle et al., 2014; Menke et al., 2017; Léger et al., 2022). Controlled experiments that systematically vary flow conditions while maintaining consistent chemistry and lithology would help assess the robustness of the identified regime transitions and extend the framework to a broader range of reactive transport conditions. Our ongoing work aims to address this objective by combining dissolution experiments with real-time imaging over a broad range of flow rates, enabling direct tracking of reaction-front evolution and comparison with the regime organisation identified here.

Conclusions

This study reanalyses dissolution experiments across multiple fluid-rock systems to identify key controls on dissolution patterns in porous media. Across large variations in fluid chemistry, lithology, and experimental conditions, the analysed systems show a consistent organisation when

expressed in terms of reactivity persistence scale (L_E), and reaction-front velocity (V_f), and Péclet number (P_e). Compact dissolution occurs at low L_E and low V_f, followed by a progression through conical, dominant, and ramified wormholing as fluid reactivity persists farther into the porous medium and the reaction front advances more rapidly. Uniform dissolution occurs at highest L_E and V_f, where reactivity is distributed over a broader region of the porous medium.

This consistent progression indicates that the persistence of fluid reactivity and the rate of reaction-front propagation capture common physical controls on dissolution-pattern development across chemically and structurally different systems. By separating the effects of reaction kinetics and fluid reaction capacity, the $L_E - V_f$ framework provides a more physically interpretable description of dissolution behaviour than conventional Péclet-Damköhler scaling alone. The identified regime organisation enables prediction of dissolution morphology and provides a basis for evaluating how changes in flow and reaction conditions influence the transition from compact to localised and ultimately distributed dissolution.

Further controlled experiments, particularly for carbonate systems interacting with CO_2-rich fluids, will allow the framework to be tested over a wider range of conditions and strengthen its application to the design, optimisation, and risk assessment of subsurface processes, particularly geological CO_2 storage.

Acknowledgements

A.V acknowledges funding from the Shell InFUSE Prosperity Partnership and the Engineering and Physical Sciences Research Council (EPSRC, grant no EP/V038044/1) and also funding from

MICIU/AEI /10.13039/501100011033 and from the FSE+ through the 'Juan de la Cierva' fellowship (reference JDC2024-053739-I). S.K. acknowledges support from Shell and the Royal Academy of Engineering under the Research Chairs and senior Research Fellowships programme

References

Bachu, S. (2003). Screening and ranking of sedimentary basins for sequestration of CO_2 in geological media in response to climate change. *Environmental Geology*, 44(3), 277-289. https://doi.org/10.1007/s00254-003-0762-9

Buijse, M., Glasbergen, G. (2005). A semiempirical model to calculate wormhole growth in carbonate acidizing. In *SPE* Annual Technical Conference and Exhibition? (pp. SPE-96892). https://doi.org/10.2118/96892-MS

Dold, B. (2017). Acid rock drainage prediction: A critical review. *Journal of Geochemical Exploration*, 172, 120–132. https://doi.org/10.1016/j.gexplo.2016.09.014

Phillips, O. M. (2009). Geological fluid dynamics: sub-surface flow and reactions. *Cambridge University Press.*

Fredd, C. N., Fogler, H. S. (1998a). Alternative stimulation fluids and their impact on carbonate acidizing. *SPE Journal*, 3(01), 34-41.https://doi.org/10.2118/31074-PA

Fredd, C. N., Fogler, H. S. (1998b). Influence of transport and reaction on wormhole formation in porous media. *AIChE Journal*, 44(9), 1933-1949. https://doi.org/10.1002/aic.690440902

Fredd, C. N., Fogler, H. S. (1998c). The influence of chelating agents on the kinetics of calcite dissolution. *Journal of Colloid and Interface Science*, 204(1), 187–197. https://doi.org/10.1006/jcis.1998.5535

Frisia, S., Borsato, A. (2010) Karst. *Developments in sedimentology*. 61, 269-318. https://doi.org/10.1016/S0070-4571(09)06106-8

Gaus, I. (2010) Role and impact of CO_2–rock interactions during CO_2 storage in sedimentary rocks. International Journal of Greenhouse Gas Control 4, 73–89. https://doi.org/10.1016/j.ijggc.2009.09.015.

Golfier, F., Zarcone, C., Bazin, B., Lenormand, R., Lasseux, D., Quintard, M. (2002). On the ability of a Darcy-scale model to capture wormhole formation during the dissolution of a porous medium. *Journal of fluid Mechanics*, 457, 213-254. https://doi.org/10.1017/S0022112002007735

Hale, S., Trindade Pedrosa, E., Jacob, A., Reinhardt, M., Enzmann, F., Kersten, M., Blum, P. (2022). Upscaling calcite dissolution rates in a tight reservoir sandstone. *Environmental Earth Sciences*, 81(11), 303. https://doi.org/10.1007/s12665-022-10399-5

Kurganskaya, I., Luttge, A. (2021). Mineral dissolution kinetics: Pathways to equilibrium. *ACS Earth and Space Chemistry*, 5, 1657–1673. https://doi.org/10.1021/acsearthspacechem.1c00017

Kurotori, T., Zahasky, C., Hejazi, S. A. H., Shah, S. M., Benson, S. M., Pini, R. (2019). Measuring, imaging and modelling solute transport in a microporous limestone. *Chemical Engineering Science*, 196, 366-383.

Leclère, H., Faulkner, D., Llana-Fúnez, S., Bedford, J., Wheeler, J. (2018). Reaction fronts, permeability and fluid pressure development during dehydration reactions. *Earth and Planetary Science Letters*, 496, 227-237. https://doi.org/10.1016/j.epsl.2018.05.005

Leger, M., Roubinet, D., Jamet, M. and Luquot, L. (2022). Impact of hydro-chemical conditions on structural and hydro-mechanical properties of chalk samples during dissolution experiments. Chemical Geology, 594, p.120763. https://doi.org/10.1016/j.chemgeo.2022.120763

Machel, H.G. (1999) Effects of groundwater flow on mineral diagenesis, with emphasis on carbonate aquifers. *Hydrogeology Journal* 7, 94-107. https://doi.org/10.1007/s100400050182

Machel, H.G. (2004) Concepts and models of dolomitization: a critical reappraisal. *Geological Society, London, Special Publications* 235(1), 7-63. https://doi.org/10.1144/GSL.SP.2004.235.01.02

Menke, H.P., Bijeljic, B., Blunt, M.J. (2017). Dynamic reservoir-condition microtomography of reactive transport in complex carbonates: Effect of initial pore structure and initial brine pH. *Geochimica et Cosmochimica Acta*, 204, 267-285. https://doi.org/10.1016/j.gca.2017.01.053

Noiriel, C., Luquot, L., Madé, B., Raimbault, L., Gouze, P., Van der Lee, J. (2009). Changes in reactive surface area during limestone dissolution: An experimental and modelling study. *Chemical Geology*, 265(1-2), 160-170. https://doi.org/10.1016/j.chemgeo.2009.01.032

Oelkers, E. H. (1996) Physical and chemical properties of rocks and fluids for chemical mass transport calculations. *Reviews in Mineralogy* 34, 131-192. https://doi.org/10.1515/9781501509797-006

Palandri, J. L., Kharaka, Y. K. (2004). A compilation of rate parameters of water-mineral interaction kinetics for application to geochemical modeling (No. 2004-1068). *US Geological Survey.* https://doi.org/10.3133/ofr20041068

Phillips, T., Kampman, N., Bisdom, K., Inskip, N. D. F., den Hartog, S. A., Cnudde, V., Busch, A. (2020). Controls on the intrinsic flow properties of mudrock fractures: A review of their importance in subsurface storage. *Earth-Science Reviews*, 211, 103390. https://doi.org/10.1016/j.earscirev.2020.103390

Snippe, J., Gdanski, R., Ott, H. (2017). Multiphase modelling of wormhole formation in carbonates by the injection of CO_2. *Energy Procedia*, 114, 2972–2984. https://doi.org/10.1016/j.egypro.2017.03.1426

Snippe, J., Berg, S., Ganga, K., Brussee, N., Gdanski, R. (2020). Experimental and numerical investigation of wormholing during CO_2 storage and water alternating gas injection. *International Journal of Greenhouse Gas Control*, 94, 102901. https://doi.org/10.1016/j.ijggc.2019.102901

Talbot, M.S., Gdanski, R.D. (2008). Beyond the Damkohler number: a new interpretation of carbonate wormholing. In *SPE* Europec, featured at *EAGE* Conference and Exhibition? (pp. SPE-113042). https://doi.org/10.2118/113042-MS

Vafaie, A., Cama, J., Soler, J.M., Kivi, I.R., Vilarrasa, V. (2023a). Chemo-hydro-mechanical effects of CO_2 injection on reservoir and seal rocks: A review on laboratory experiments. *Renewable and Sustainable Energy Reviews*, 178, 113270. https://doi.org/10.1016/j.rser.2023.113270

Vafaie, A., Cama, J., Soler, J.M., Grgic, D., Vilarrasa, V. (2023b). Chemo-hydro-mechanical effects of CO2 injection into a permeable limestone. *International Journal of Coal Geology*, 278, 104359. https://doi.org/10.1016/j.coal.2023.104359

Vafaie, A., Soler, J.M., Cama, J., Kivi, I.R., Vilarrasa, V. (2025). A 3D Darcy-scale reactive transport modeling of experimental wormhole formation in limestone under geological CO_2 storage conditions. *International Journal of Greenhouse Gas Control*, 146, 104452. https://doi.org/10.1016/j.ijggc.2025.104452

Vialle, S., Contraires, S., Zinzsner, B., Clavaud, J.B., Mahiouz, K., Zuddas, P., Zamora, M. (2014). Percolation of CO_2-rich fluids in a limestone sample: evolution of hydraulic, electrical, chemical, and structural properties. *Journal of Geophysical Research Solid Earth* 119, 2828–47. https://doi.org/10.1002/2013JB010656.